Toward Mitigating Stratified Tropospheric Delays in Multitemporal InSAR: A Quadtree Aided Joint Model

Hongyu Liang, *Student Member, IEEE*, Lei Zhang, *Member, IEEE*, Xiaoli Ding, Zhong Lu, *Senior Member, IEEE*, and Xin Li

***Abstract*— Tropospheric delays (TDs) in differential interferometric synthetic aperture radar (InSAR) measurements are mainly caused by spatial and temporal variation of pressure, temperature, and humidity between SAR acquisitions. These delays are described as one of the primary error sources in InSAR observations. Although independent atmospheric measurements have been used to correct TDs, their sparse spatial or temporal resolution requires interpolation, leading to uncertainties in the corrected interferograms. The performance of the conventional phase-based correction method is weakened by the presence of confounding signals (e.g., TDs, deformation, and topographic errors) and spatial variability of the troposphere. Here, we propose a method that can simultaneously estimate stratified TDs together with parameters of deformation and topographic error based on their distinct spatial–temporal correlation. Spatial variability of the relationship between TDs and topographic height is addressed through localized estimation in windows divided by quadtree according to height gradient. We demonstrate the performance of the proposed method with both simulated and real data sets. In addition, both advantages and disadvantages of this method are addressed.**

***Index Terms*— Interferometric synthetic aperture radar (InSAR), least squares, tropospheric delays (TDs).**

I. Introduction

INTERFEROMETRIC synthetic aperture radar (InSAR) can provide abundant observations with high spatial resolution and precision, and has been widely applied to identify and/or measure ground deformation [1]–[5]. In recent years, considerable progress has been made to model multitemporal InSAR (MTInSAR) measurements for accurate deformation mapping [6]–[11]. The InSAR phase measurement represents a superposition of multiple signals including deformation, topographic error, satellite orbital inaccuracy, and atmospheric propagation delays. To accurately retrieve the deformation field, separating the deformation signal from the other phase components is critical, especially the atmospheric propagation delays that can impose notable errors in deformation measurements [12]–[18].

Atmospheric delays are in general divided into ionospheric and tropospheric terms [19], [20]. Delays in ionosphere are caused by spatial and temporal disturbances of free electron density. The ionospheric effect is mostly observed by long-wavelength SAR sensors caused by the dispersive property of atmospheric medium [21], [22]. In contrast, tropospheric delays (TDs) are characterized as nondispersive effects resulting from variations in pressure, temperature, and humidity. The total TDs are considered as a combined result of turbulence mixing in the neutral atmosphere and stratified delays in the lower part of the troposphere. The first component, turbulence mixing in the neutral atmosphere, varies randomly in space and time, while the stratified delays in the lower part of the troposphere are generally distributed according to the topography, leading to dependence on elevation. In this paper, we specifically focus on correcting the stratified component of TDs in MTInSAR measurements.

Different strategies have been developed to estimate and correct TDs in InSAR measurements. One group of strategies directly predicts tropospheric signals from external information. These methods include the use of local or global weather models [18], [20], [23], [24], large GPS network data [25]–[27], and satellite multispectral imagery [28], [29], such as Moderate Resolution Imaging Spectroradiometer and Medium Resolution Imaging Spectrometer. Combined methods that use satellite spectrometers together with GPS data or weather models to produce atmospheric delay maps on SAR acquisition dates [17], [30], [31] have also been developed. However, GPS-based correction is limited by the sparse distribution of GPS stations in remote areas. Image-based correction method requires calibration and can only operate under cloud-free and daylight conditions. Spectral observations and weather model measurements have the limitation of lower spatial resolution. In addition, spectral observations might not be temporally synchronized with SAR acquisitions and therefore need interpolation, leading to uncertainties in estimated tropospheric signals [32]–[34].

Another group of methods focuses on mitigating or correcting delays solely based on InSAR data itself. Typical methods involve averaging N independent interferograms [35] or performing spatiotemporal filters on interferometric phase stack [6], [7], [9], [36]. These methods can reduce phase

Manuscript received November 13, 2017; revised March 6, 2018 and May 21, 2018; accepted June 26, 2018. Date of publication August 2, 2018; date of current version December 24, 2018. This work was supported in part by the National Nature Science Foundation of China under Grant 41774023 and Grant 41304011 and in part by the Research Grants Council of Hong Kong under Grant PolyU 152232/17E, Grant PolyU 152214/14E, and Grant PolyU 152043/14E. *(Corresponding author: Lei Zhang.)*

H. Liang, L. Zhang, X. Ding, and X. Li are with the Department of Land Surveying and Geo-Informatics, The Hong Kong Polytechnic University, Hong Kong (e-mail: allenhongyu.liang@connect.polyu.hk; lslzhang@polyu.edu.hk; xl.ding@polyu.eud.hk; vivianyoxi@gmail.com).

Z. Lu is with the Roy M. Huffington Department of Earth Sciences, South Methodist University, Dallas, TX 75275, USA (e-mail: zhonglu@sum.edu).

Color versions of one or more of the figures in this paper are available online at http://ieeexplore.ieee.org.

Digital Object Identifier 10.1109/TGRS.2018.2853706

variance induced by atmospheric delays, provided that atmospheric delays are temporally uncorrelated and ground deformation is stationary over SAR observation periods. Meanwhile, the stratified component of TDs in interferograms can be empirically estimated from the best-fitting linear relation between the phase delay and the topography using [14], [20], [32]

$$\Delta\emptyset_{\text{trop}} = K \times \Delta h + \emptyset_0 \tag{1}$$

where $\Delta\emptyset_{\text{trop}}$ and Δh denote the tropospheric phase delay and elevation difference, K represents the delay/elevation ratio, and $\emptyset_0$ represents the intercept, which can be neglected when (1) is applied to the whole interferogram. Such linear height correction has been used to reduce topography-dependent phase delays, yet its performance is weakened by two limitations. One is the contamination by other signals (e.g., deformation and topographic error) which can bias the estimation of delay/elevation ratio K. Improved methods are available to remove the deformation signal by using, for example, *a priori* model of ground motion [15], [16] or a multiscale approach to select a spatial band insensitive to deformation [32] before the estimation of K. But these methods are prone to overcorrected phase delays when displacement is correlated with topography [17] and the band selection requires empirical information which is sensitive to outliers. The second limitation stems from the fact that a unified delay/elevation ratio cannot be applied for the whole extent of the SAR scene due to spatial variability of tropospheric property. Some efforts have been devoted to overcoming this by using either a piecewise linear height correction in multiple windows [13] or a spatially variable power law approach [37]. However, the former method ignores the bias of intercept $\emptyset_0$ which needs a common reference in different windows [34], [37], while the power law function is sensitive to the tradeoff between estimated parameters and deformation or turbulence signals [20], [34].

The primary goal of this paper is to develop a new TD correction method that can resolve the limitations associated with abovementioned approaches. By jointly estimating spatially varying TDs together with deformation and topographic error under the framework of MTInSAR, the proposed method can more accurately isolate TDs from other signals. Moreover, the proposed method is highly adaptive for a large set of interferograms since it is based on an interferogram stack rather than a single image pair. Because the relationship with topographic height might vary from place to place, the stratified delays should be modeled locally. The criterion for local window segmentation has not previously been explored. We propose here a quadtree-based strategy for window segmentation, which can adaptively determine the window size with the predefined allowable height gradient. In each local window, deformation and topographic errors are parameterized according to the relationship with temporal and spatial baselines, respectively, and TDs are simultaneously modeled by following their dependence on topography. We implement our model and parameter estimation under the framework proposed by Zhang *et al.* [8], where observations are phase difference at arcs (i.e., coherent point pairs) without the need of phase unwrapping, accompanied by a phase ambiguity detector designed to remove arcs having phase integers. Sections II–IV are dedicated to describing the details of the method and evaluating the performance from synthetic and real data sets.

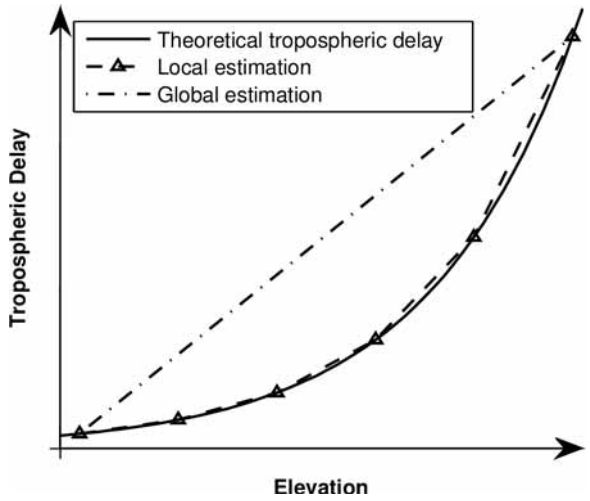

Fig. 1. Schematic of estimation for tropospheric signal. The black line shows an example of TD that varies as a nonlinear function of elevation [16], [37]. Such a delay cannot be modeled by conventional linear method (i.e., the dotted-dashed line), which, however, can be well approximated by polylines (i.e., the dotted-dashed line with triangle). These polylines have fixed slopes within certain gradients.

II. Methodology

A. Window Segmentation

The starting point of this method is selecting interferometric pairs with short temporal and spatial baselines. In each interferogram, phase ramps induced by orbital inaccuracy are preliminarily removed by fitting 2-D polynomials [10], [38], [39]. Considering the spatial variability of troposphere signal, the whole scene of the interferogram is divided into multiple windows. Regular use of square windows has been widely employed for this purpose [13], [37], [40]. However, such strategy defines the same spatial size over the whole image without accounting for the elevation variation within each window, possibly resulting in unsuitable windows. For example, if the size is too small, there might be some windows that are entirely occupied by the turbulent component of atmospheric delays, degrading the reliability of estimated delay-elevation ratios [34] and increasing the computational burden, while if the size is unsuitably large, there might be some windows with a large elevation gradient, making it insufficient to model the stratified component linearly. Instead, considering that the stratified delay has a strong relationship with elevation, which can be modeled linearly within a certain height difference (Fig. 1), we conduct window segmentation according to height gradient by quadtree. Only those windows with a large height gradient are further divided into quadrant windows; thus, the turbulence will not occupy the entire estimation area and preserve the linearity of tropospheric variation. The procedure of window segmentation is described as follows.

1) Initialize coarse windows for the whole scene in radar coordinate system.

2) Compute the elevation range within each window.
3) Identify windows whose elevation ranges exceed threshold Z and divide the selected windows into four quadrants.
4) Repeat steps 2 and 3 and terminate when the size of the divided window is smaller than threshold S.

To maintain the spatial consistency, adjacent windows have an overlap of 25% window size. The threshold S for the smallest window size and Z for the elevation range can be determined from *a priori* information. Theoretically, since TDs are caused by the air refractivity gradients of the neutral troposphere along the vertical due to variations of pressure, temperature, humidity, and water vapor content across the scene, the delay variation in space is correlated with these components. For the smallest window size, considering the complicated variation of troposphere in space, the lower limit for the smallest window size S can be set as 2 km, as smaller length scale ($S < 2$ km) is relatively insensitive to larger scale tropospheric signals [32]. For elevation range, a too small range may lead to insufficient observations in divided window, while unsuitably large range might introduce nonlinear variation of troposphere. In this paper, 1000 m could be a conservative threshold of elevation range where the troposphere varies linearly with elevation, since previous studies have shown that delay/elevation ratio remains stable within 900–2000 m [15], [20].

B. Joint Estimation in Local Window

Once window segmentation is finished, local Delaunay triangulation [8] is employed to densely construct arcs (i.e., point pairs) from coherent points within each window. The relationship between stratified TDs and elevation in an individual SAR acquisition is taken as linear within a localized area. The relative phase delays in an interferometric pair can be represented as the difference of phase delays in master and slave SAR acquisitions, each being described by (1) with respect to a reference acquisition. Considering that interferograms are the linear combinations of SAR images, for simplicity, we assume here that the stratified TDs in the optionally selected reference image is zero and use the resulting images to generate the delays in all of the selected interferograms. By doing so, the number of parameters to be estimated will be reduced. The phase delay at coherent point p with respect to the reference SAR acquisition is expressed as

$$\emptyset^i_{\text{trop,slc},p} = h_p \times K^i_{\text{slc}} + \emptyset_0. \tag{2}$$

The phase delay difference between coherent points p and q can be written as

$$\Delta\emptyset^i_{\text{trop,slc},p,q} = (h_p - h_q) \times K^i_{\text{slc}} \tag{3}$$

where i is denoted as the window number, K^i_{slc} is the best-fitting linear coefficient within the window, and h_p and h_q represent the elevation of points p and q, respectively. Since points p and q are with respect to the same reference in the local window, intercept $\emptyset_0$ is canceled out during the differencing operation. If there are G arcs constructed in the ith local window, the relative phase delays at all arcs in an SAR acquisition can be written as

$$\frac{\Delta\Phi^i_{\text{trop,slc}}}{G \times 1} = \frac{dh^i}{G \times 1} \times \frac{K^i_{\text{slc}}}{1 \times 1} \tag{4}$$

where dh^i is the vector of elevation difference between points that form all arcs in the local window. Considering that there are M interferograms generated from N SAR images, phase components due to TDs in the ith local window at all arcs from M interferograms can be denoted by

$$\frac{\Delta\Phi^i_{\text{trop}}}{(G \times M) \times 1} = \frac{B^i_{\text{trop}}}{(G \times M) \times (N-1)} \times \frac{P^i_{\text{trop}}}{(N-1) \times 1} \tag{5}$$

with

$$\frac{B^i_{\text{trop}}}{(G \times M) \times (N-1)} = \frac{dh^i}{G \times 1} \otimes \frac{F}{M \times (N-1)} \tag{6}$$

where $\Delta\Phi^i_{\text{trop}}$ represents $(G \times M) \times 1$ vector including all phase differences induced by TDs in ith local window from M interferograms, P^i_{trop} contains all TD coefficients with respect to reference SAR image, and $\otimes$ denotes the Kronecker tensor product. F is the linear conversion matrix from single SAR image to interferometric pair; it has the form as

$$F = \begin{bmatrix} 1 & 0 & -1 & \cdots & 0 \\ 0 & 1 & \cdots & -1 & 0 \\ \vdots & \vdots & \vdots & \vdots & \vdots \\ 0 & 0 & 1 & 0 & -1 \end{bmatrix}_{M \times (N-1)} \tag{7}$$

where 1 and -1 indicate master and slave SAR images, respectively, in an interferometric pair. Note that since the TD in reference SAR image is usually taken as zero without loss of generification, the corresponding column in F has been removed.

As mentioned previously, apart from TDs, InSAR observations are also subject to deformation and topographic error. These errors may influence the estimation of TDs in interferograms. To account for them, in the jth interferogram for an arbitrary coherent point p, the deformation rate (v_p) and topography error (Δh_p) with respect to reference point can be modeled by

$$\emptyset^i_{\text{defo+topo},p} = \begin{bmatrix} -\frac{4\pi}{\lambda} \times T_j & -\frac{4\pi}{\lambda} \times \frac{B_{\perp,j}}{r \times \sin\theta} \end{bmatrix} \times \begin{bmatrix} v_p \\ \Delta h_p \end{bmatrix} \tag{8}$$

where λ is the radar wavelength, r is the slant range distance from SAR satellite to ground coherent point p, θ is the local incident angle $B_{\perp,j}$ and T_j represent the interferogram's spatial and temporal baselines, respectively. Note that for simplicity here we define the deformation model as a linear term. In other cases, nonlinear deformation can be empirically modeled by quadratic and cubic polynomials as well as seasonal functions [7], [8], [41]. Considering M interferometric pairs, phase contributions due to deformation and topography error can be expressed as

$$\frac{\Phi^i_{\text{defo+topo},p}}{M \times 1} = \frac{\beta^i_{\text{defo+topo},p}}{M \times 2} \times \frac{P^i_{\text{defo+topo},p}}{2 \times 1} \tag{9}$$

where $P^i_{\text{defo+topo},p} = [\Delta h_p \ v_p]^{\text{T}}$, and $\beta^i_{\text{defo+topo},p}$ is a design matrix converting deformation rate and topography error to interferometric phases. When there are G arcs constructed from L coherent points in the ith local window, phase components due to deformation and topographic error from M interferograms are denoted by

$$\frac{\Delta\Phi^i_{\text{defo+topo}}}{(G\times M)\times 1} = \frac{B^i_{\text{defo+topo}}}{(G\times M)\times 2(L-1)} \times \frac{P^i_{\text{defo+topo}}}{2(L-1)\times 1} \quad (10)$$

with

$$\frac{B^i_{\text{defo+topo}}}{(G\times M)\times 2(L-1)} = \frac{C^i}{G\times(L-1)} \otimes \frac{\beta^i_{\text{defo+topo}}}{M\times 2} \quad (11)$$

where $\Delta\Phi^i_{\text{defo+topo}}$ represents $(G\times M)\times 1$ vector including all phase differences induced by deformation and topographic error in ith local window from M interferograms. $P^i_{\text{defo+topo}}$ represents 2-D vector of deformation rate and topographic error for $L-1$ coherent points in the ith local window. Note that the parameters of one reference point have been assumed to be known. C^i is the network matrix relating coherent points and arcs in the ith local window, in which the column associated with the reference point has been removed. It has a form as

$$C^i = \begin{bmatrix} 1 & 0 & -1 & \cdots & 0 \\ 0 & 1 & \cdots & -1 & 0 \\ \vdots & \vdots & \vdots & \vdots & \vdots \\ 0 & 0 & 1 & 0 & -1 \end{bmatrix}_{G\times(L-1)} \quad (12)$$

where 1 indicates the starting point and -1 refers to the ending point along an arc.

Since the proposed method aims to simultaneously estimate TDs, deformation, and topography error, the joint model can be derived by combining (5) and (10)

$$\frac{\Delta\Phi^i}{(G\times M)\times 1} = B^i \times P^i + \frac{R^i}{(G\times M)\times 1} \quad (13)$$

with

$$\begin{aligned} B^i &= \left[\, B^i_{\text{defo+topo}} \ B^i_{\text{trop}} \,\right] \\ P^i &= \left[\, P^i_{\text{defo+topo}} \ P^i_{\text{trop}} \,\right]^{\text{T}} \end{aligned} \quad (14)$$

where $\Delta\Phi^i$ represents $(G\times M)\times 1$ vector including all observations of phase differences in a joint model. R_i represents corresponding phase residual vector induced by decorrelation effects, unmodeled deformation, and turbulence signals. By solving (13), we can obtain TD ratio, deformation rate, and topography error at the same time. It should be noted that in (13), the design matrix on the right side and the observation vector on the left side contain the estimation information of all arcs in a local window; it is difficult to use conventional least squares to solve such a large sparse linear system. Alternatively, we can adopt sparse matrix factorization to derive the solution. One typical method refers to an iterative process with the constraint $\min \left\| R^i \right\|^2$ based on the Golub–Kahan bidiagonalization [42].

Since observations in (13) are calculated from the difference of wrapped phases, we assume that there are some phase ambiguities in the observations and they should be removed before performing precise estimation. Under this assumption, we adopt the outlier detector proposed in [8] to identify the arcs with phase ambiguities from the residual of (13) after initial solution. The detector can be expressed as [8], [10]

$$\max(|r_g|) > \Gamma, \quad g = 1,\ldots,G \quad (15)$$

where r_g represents the vector of phase residual of gth arc in R^i and Γ denotes the threshold of phase residual. Once the arcs with phase ambiguities are identified and eliminated, isolated points are detected and discarded to avoid rank deficiency in design matrix B^i. Observations $\Delta\Phi^i$ and design matrix B^i in (13) will also be updated after removing points and arcs. The unknown coefficients are obtained by conducting sparse matrix factorization again. Considering E points and F arcs are remained after phase ambiguity detection, the phase differences at arcs after removal of tropospheric signals can be derived by

$$\frac{\widetilde{\Delta\Phi}^i_o}{(F\times M)\times 1} = \frac{\widetilde{\Delta\Phi}^i}{(F\times M)\times 1} - \frac{\widetilde{B}^i_{\text{trop}}}{(F\times M)\times(N-1)} \times \frac{\widetilde{P}^i_{\text{trop}}}{(N-1)\times 1} \quad (16)$$

with

$$\frac{\widetilde{\Delta\Phi}^i_o}{(F\times M)\times 1} = \left[\, \widetilde{\Delta\emptyset}^i_{o,1} \ \widetilde{\Delta\emptyset}^i_{o,2} \cdots \ \widetilde{\Delta\emptyset}^i_{o,j} \cdots \ \widetilde{\Delta\emptyset}^i_{o,M} \,\right]^{\text{T}} \quad (17)$$

where $\widetilde{\Delta\Phi}^{\text{i}}$, $\widetilde{B}^i_{\text{trop}}$, and $\widetilde{P}^i_{\text{trop}}$ represent updated terms in (13), and $\widetilde{\Delta\Phi}^i_{\text{o}}$ represents the phase difference at all remained arcs from M interferograms after correcting TDs in the ith local window.

C. Final Solution

After performing joint estimation in each local window, the stratified tropospheric phase delays are removed locally. The phase differences at arcs after the removal of TDs are derived over the whole scene. Some arcs might within the overlapped area between adjacent windows might have different phase difference values. This is mainly because the spatial variation of troposphere makes the delay/elevation ratios vary in different windows. To derive optimized results, we choose to retain the arcs in overlaps that have the smallest residuals obtained by (13). Once redundant arcs are removed, corrected phases at coherent points are obtained by spatial integration with respect to a reference point. For each interferogram, the corrected phase differences at arcs and phase values at points can be linked by

$$\widetilde{\Delta\emptyset}^i_{o,j} = C \times X_j \quad (18)$$

where X_j represents the jth corrected interferogram for TDs, and C denotes the conversion matrix relating coherent points to arcs in whole scene. Note that the column corresponding to the reference point in C has been removed. Thus, (18) can be solved using least squares

$$X_j = \left(C^{\text{T}} W C\right)^{-1} C^{\text{T}} W \widetilde{\Delta\emptyset}^i_{o,j}. \quad (19)$$

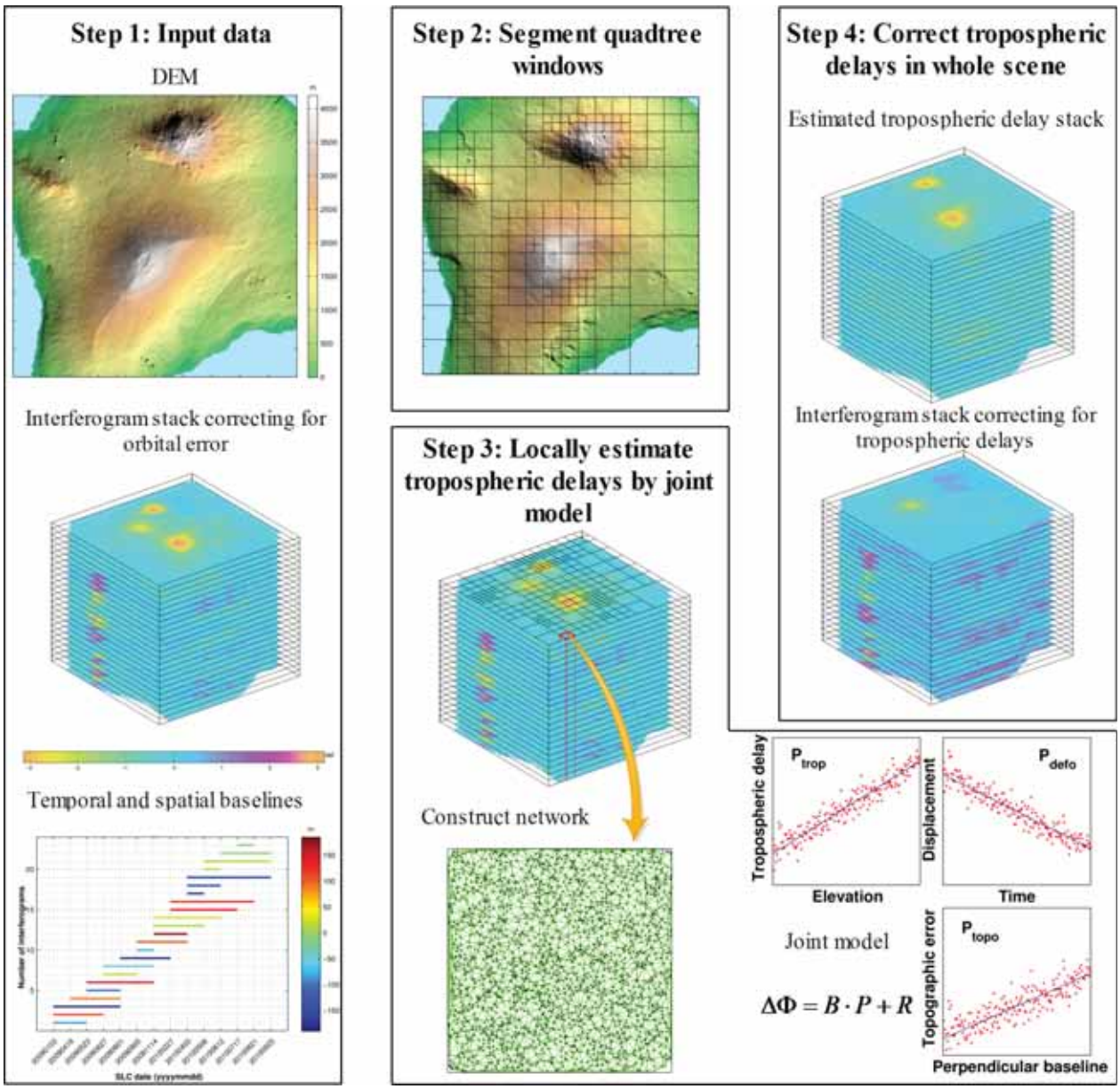

Fig. 2. Step-by-step routine for the proposed TD correction.

D. Algorithm Flowchart

The algorithm flowchart is shown in Fig. 2, and the whole procedure of the developed method is described as follows.

1) Prepare input data sets, including digital elevation model (DEM) of the study area, multitemporal interferogram stack, and associated spatiotemporal baselines.
2) Divide the whole scene into quadrant windows according to height gradient by quadtree.
3) Within each local window, construct point network and jointly parameterize deformation, topographic error, and height-dependent TDs. Outliers with phase ambiguities are detected and removed based on the estimated residuals after initially solving the joint model; a second estimation to correct TD at arcs is then performed.
4) Combine all arcs from local windows to the whole scene and integrate estimated TDs and corrected phases from arcs to points.

III. Synthetic Data Test

To evaluate the performance of the proposed method, we conducted a simulation test using synthetic data consisting of 14 SAR images based on the topography of the island of Hawai'i. The benefit of using a synthetic data set is that the estimated tropospheric phase delays can be compared with the true values that are often unknown in real cases. During the test, we generated 202 530 coherent points in the test area with a spatial size of 92.2 km × 87.7 km and elevation range of 4.2 km. The large coverage and high relief allow simulation of spatial variability for tropospheric signals. We assumed that the phase ramps induced by orbital errors have been removed before estimation, so the signal components considered in the synthetic interferogram include tectonic deformation, stratified TD, topographic error, atmospheric turbulence, and random noise. The ground deformation field was constructed by using a Mogi model based on a point source in an elastic

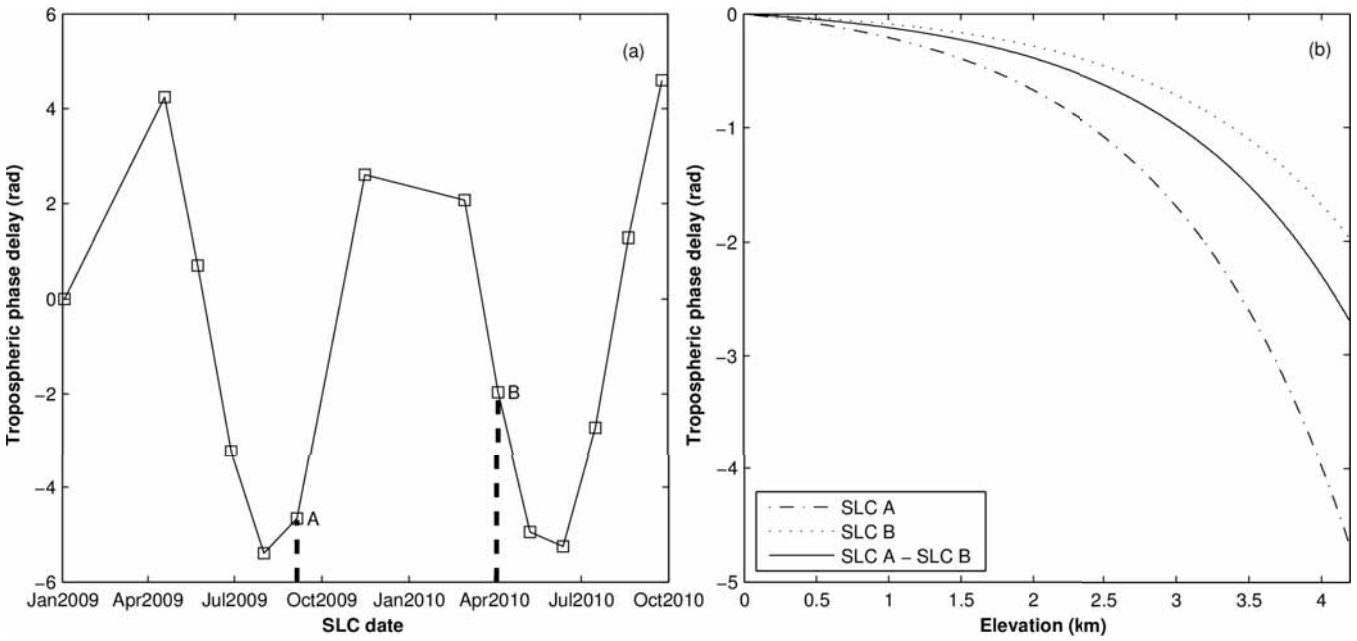

Fig. 3. (a) Temporal evolution of tropospheric signals at SAR acquisitions. (b) Relationship between TD and elevation in simulated interferogram.

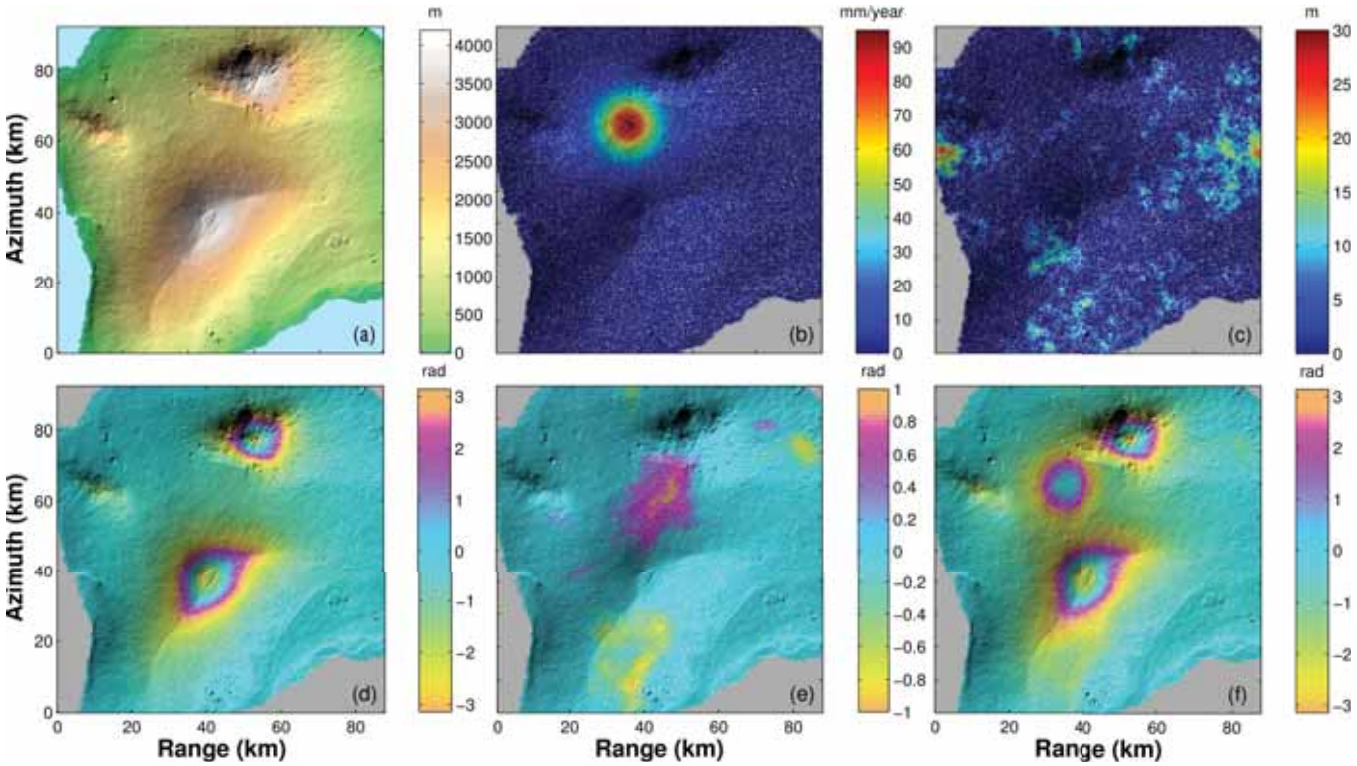

Fig. 4. Main components for construction of synthetic interferogram. (a) Topography of island of Hawai'i. (b) Deformation rate. (c) Topographic error. (d) Topography-related TDs. (e) Turbulence mixing. (f) Final synthetic interferogram. One color cycle corresponds to 5.6 cm in LOS direction.

half-space [43]. We defined that the central depth of point source is 8.7 km and the maximum deformation rate is 95 mm/year along SAR line of sight (LOS) direction. To simulate the spatial variability of stratified troposphere, we used an exponential function to express the relationship between phase delay and topography [17], [20]. Considering the temporal fluctuation, interannual sine function was used to simulate the seasonal variation of troposphere [20], [23]; therefore, for a point with elevation h at a given SAR acquisition, the tropospheric phase delay can be empirically expressed as

$$\emptyset_{\text{trop}} = \frac{(\emptyset_h - \emptyset_{h,\min}) \times R}{\emptyset_{h,\max} - \emptyset_{h,\min}} \tag{20}$$

with

$$\begin{aligned} \emptyset_h &= e^h \\ R &= a + b \times \sin\left(\frac{2\pi}{T} \times t\right) \end{aligned} \tag{21}$$

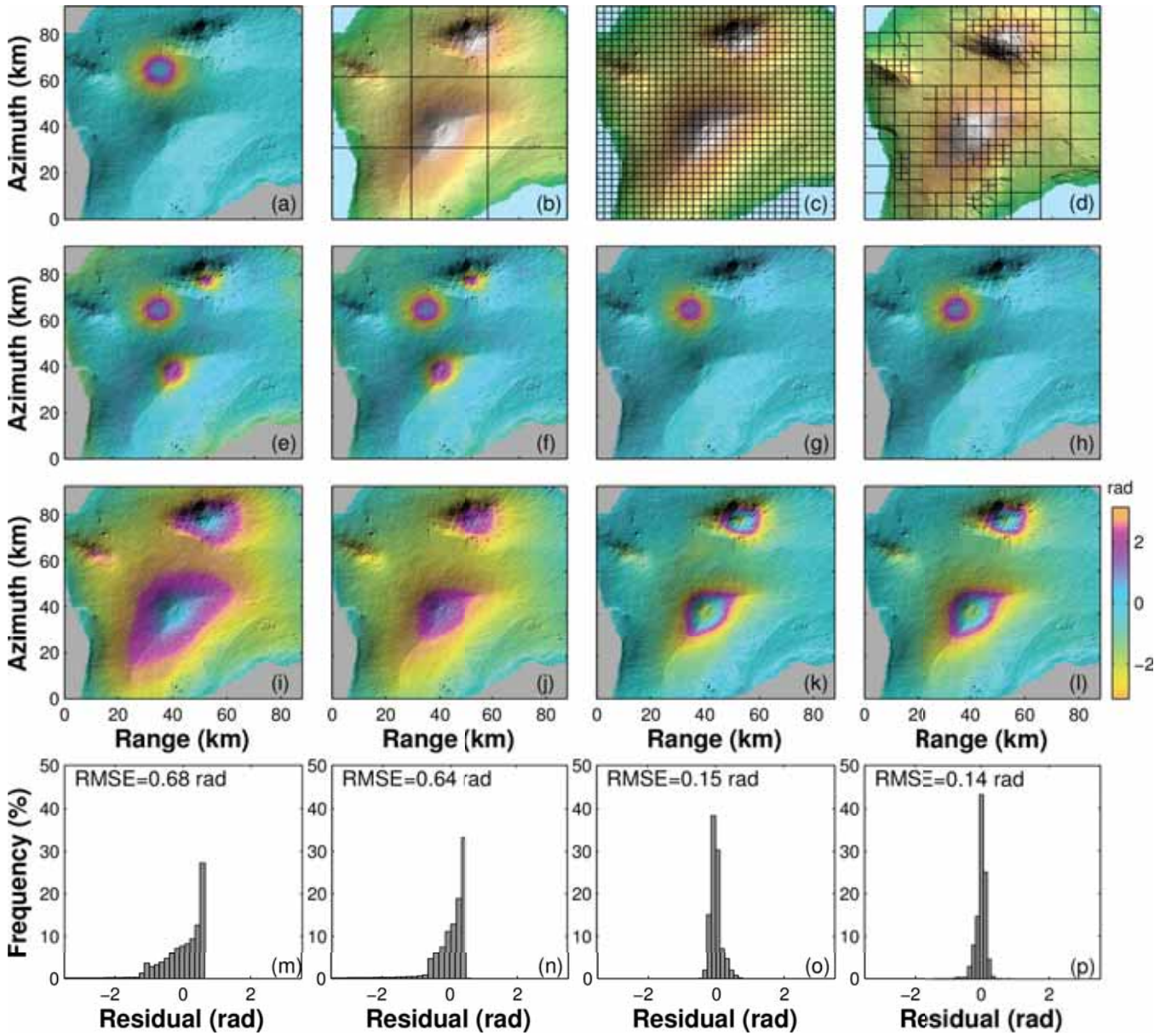

Fig. 5. Comparison of corrected results for TDs by (e), (i), and (m) conventional linear method, (f), (j), and (n) joint model with 3×3 regular windows, (g), (k), and (o) joint model with 32×32 windows, and (h), (l), and (p) joint model with quadtree windows. (a) Simulated interferogram without TDs. (b)–(d) Schematics of window segmentation in joint model. (e)–(h) Corrected interferogram for TDs by four methods. (i)–(l) Estimated TDs. (m)–(p) Distribution of residuals between synthetic and estimated TDs.

where a and b are the intercept and coefficient of sine function, respectively, t represents the SAR acquisition time, and T is the period of seasonal variation of troposphere. Fig. 3(a) presents the simulation of temporal evolution of tropospheric signal at SAR acquisitions. We produced topographic errors using fractal surface with a fractal dimension of 2.8 and defined the errors distribute between 0 and 30 m. The atmospheric turbulence in each SAR image was simulated using fractal surface with fractal dimension being 2.2 [44]. The turbulence had a maximum variation of 1 rad and occupies 30% of the whole scene. The random noise was generated in all SAR images with a mean of 0 rad and a standard deviation of 0.1 rad. During the test, we generated 23 interferograms with spatial and temporal baselines that are shorter than 200 m and 220 days. Fig. 4 shows a realization of one simulated interferogram.

Using these synthetic data sets, we implemented the quadtree-aided joint model. The smallest window size and the threshold of elevation range for window segmentation were set as 2.7 km and 1000 m, respectively. Parameters of height-dependent TDs for SAR acquisitions were estimated together with the deformation rate and the topographic error in each divided window. We derived the estimated tropospheric phase delays and phase maps after TD correction. The root mean square (rms) of simulated tropospheric phase delays was calculated as the magnitude of TDs. We then computed the difference between the estimated and simulated TDs and compared with the results from a conventional linear method

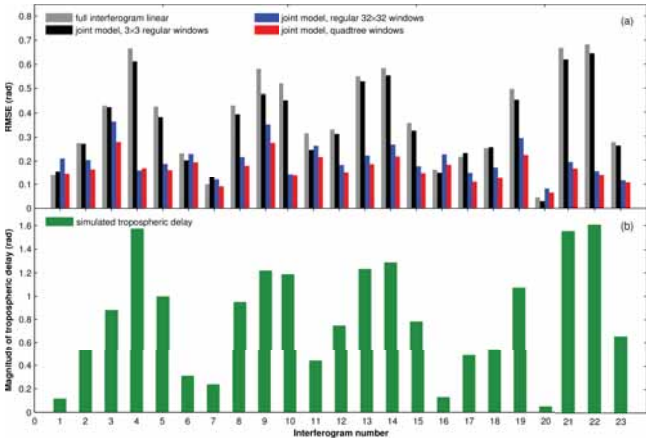

Fig. 6. (a) RMSE between estimated and simulated TDs in each interferogram. Each color corresponds to the result derived by one kind of method. (b) RMS of simulated TDs in each interferogram.

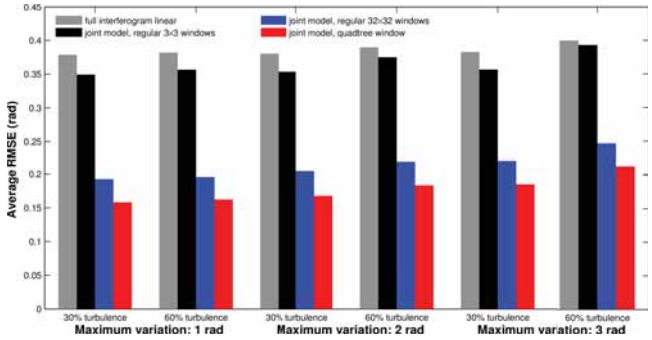

Fig. 7. Average RMSE between estimated and simulated TDs in 23 interferograms. Each color corresponds to the result derived by one kind of method.

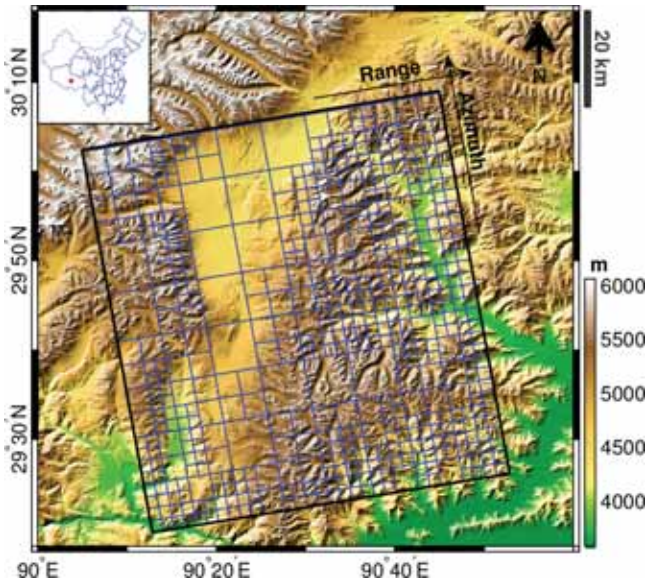

Fig. 8. Topographic map of Dangxiong of southern Tibet generated from SRTM DEM data. The black solid box outlines the study area covered by ALOS PALSAR data (Ascending Track 500). The blue solid rectangles represent the divided quadtree windows according to elevation gradient.

(see Figs. 5 and 6). The comparison results show that even under spatial variability of tropospheric properties and other confounding signals, the joint model can still provide a stable estimate of TDs. In the cases when simulated TDs are very small, the joint model-derived TDs have a slightly larger root-mean-square error (RMSE) than the results from the linear method, but still within an accepted range of error. The relatively larger deviation is mainly because when turbulence mixing overwhelms the height-related TDs across the whole scene, the linear method is less affected than the local estimation [34]. In general, regardless of magnitude of TDs, the quadtree-aided joint model can effectively correct TDs from multitemporal interferogram stack.

We also considered the impact of quadtree segmentation on joint estimation. In addition to the aforementioned quadtree, we adopted two other window segmentation strategies before proceeding to joint estimation. The SAR scene was divided into regular uniform windows using two different scenarios; one scenario used larger dimension windows of 31 km $\times$ 29 km [Fig. 5(b)], and the second used a smaller window size of 2.9 km $\times$ 2.7 km [Fig. 5(c)]. In each divided window, we implemented the same joint estimation and combined the estimation results back into the whole scene. The results obtained from the regular window segmentations were compared with the results of a quadtree-aided segmentation (Figs. 5 and 6). Interestingly, no matter which regular window size was employed, the quadtree-aided joint model tends to outperform them. In fact, it is challenging for regular window segmentation to achieve the balance between tropospheric inhomogeneity in space and reliability of local estimation. In contrast, by using two parameters (i.e., elevation range and spatial dimension), the quadtree segmentation can achieve optimal tradeoff between preserving the spatial stability of troposphere in mountainous areas and minimizing turbulent degradation in flat areas.

We further tested turbulent effects on the estimation of TDs in the proposed model. There are two major parameters that can be used to describe turbulent effects in space. One is the maximum magnitude of turbulence in phase, which was set as 1, 2, and 3 rad. The other parameter is the spatial scale of the turbulence. Here, we set it as 30% and 60% of the whole scene size, respectively. We calculated the average RMSE between the estimated and simulated TDs from 23 interferograms and plotted the results in Fig. 7. With the increase in turbulent magnitude and spatial size, no significant rise of RMSE is detected, implying that the proposed method for stratified component mitigation is insensitive to turbulence effect. This is because turbulence mixing varies randomly in space and time while the stratified delay only correlates with elevation; the use of abundant observations at arcs ensures the robustness of linear estimation in local windows.

IV. Real Data Test

A. ALOS/PALSAR Data Over Dangxiong

We tested the quadtree-aided joint model by using the Dangxiong area of southern Tibet (Fig. 8), where crustal activities are frequent due to normal faulting of the Yangdong–Gulu rift system. GPS records show that the active rift system has a left-lateral slip rate of 0.7 ± 1.1 mm/year and an opening rate

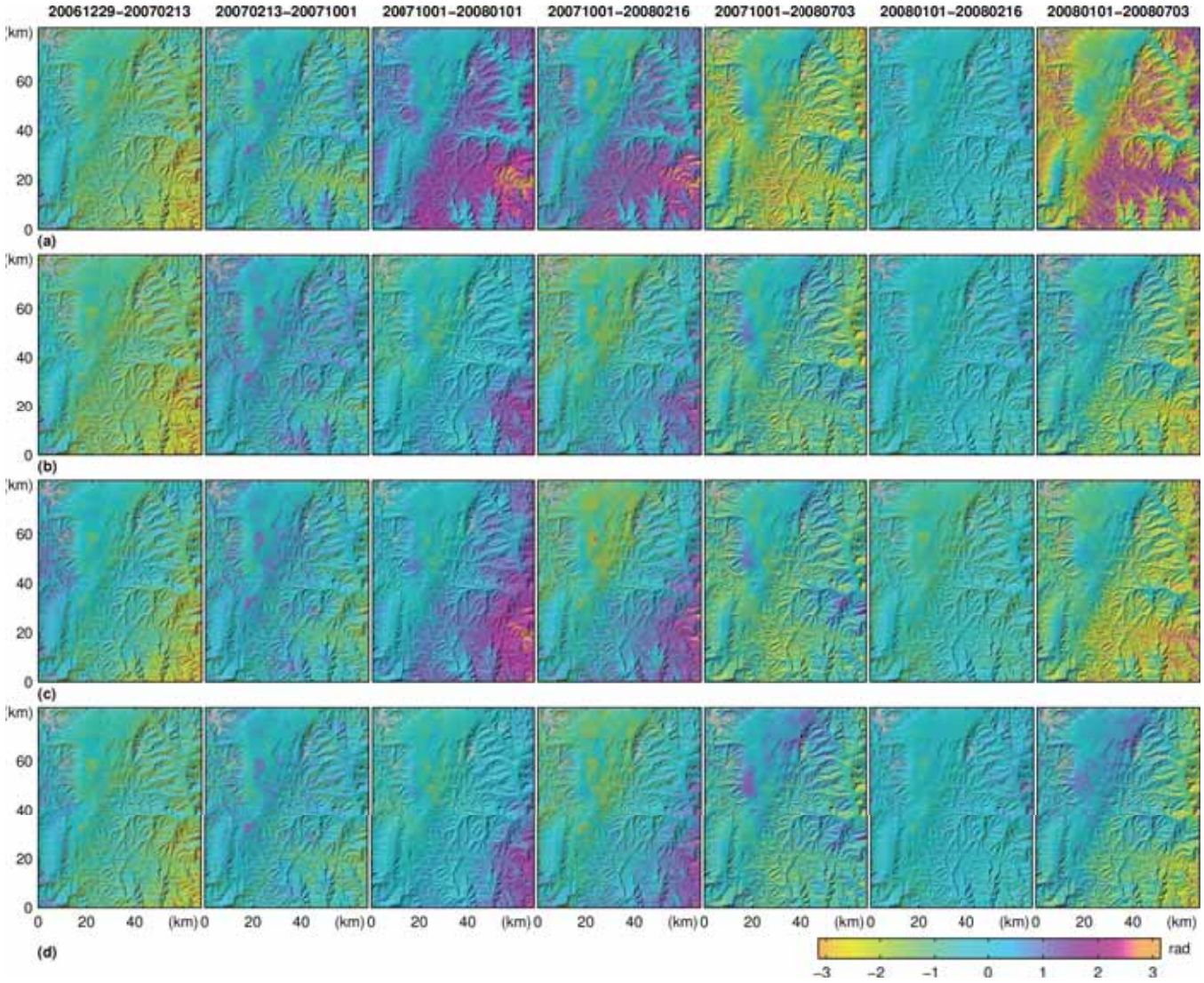

Fig. 9. Comparison of corrected interferograms over Dangxiong for ALOS/PALSAR data. (a) Wrapped interferograms before correcting TDs. (b) Wrapped interferograms after correcting TDs by linear method. (c) Wrapped interferograms after correcting TDs by ITD method. (d) Wrapped interferograms after correcting TDs by quadtree-aided joint model.

TABLE I
INTERFEROMETRIC PAIR BASELINE INFORMATION

No.	Interferometric pair	Perpendicular baseline (m)	Temporal baseline (day)
1	20061229-20070213	1552	46
2	20070213-20071007	813	230
3	20071001-20080101	192	92
4	20071001-20080216	1174	138
5	20071001-20080703	-1105	276
6	20080101-20080216	981	46
7	20080101-20080703	-1297	184

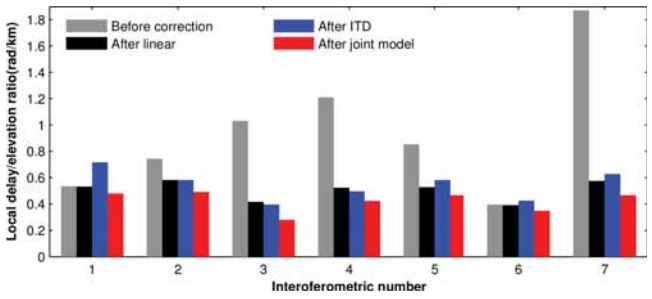

Fig. 10. Comparison of local delay/elevation ratios before and after corrections for ALOS/PALSAR data.

of 2±0.6 mm/year [45]. On October 6, 2008, an Mw 6.3 earthquake struck this area, causing large economic losses and casualties. We obtained preseismic data of six ALOS/PALSAR images (ascending track 500) acquired between December 29, 2006 and July 3, 2008. Seven interferograms were generated with the spatial and temporal baselines less than 1300 m and 330 days, respectively (Table I). As the test area has large spatial coverage (67 km × 82 km) and rugged topographic relief (3.6–6.3 km), the same TD/elevation ratio does not apply across all the regions of the interferogram. Elevation-dependent tropospheric signals still remain in the interferogram even after correction by the linear method [46]. During the processing, we selected 2697662 coherent points from multilooked interferograms with a spatial resolution of roughly 45 m. After correcting phase ramps due to orbital inaccuracy

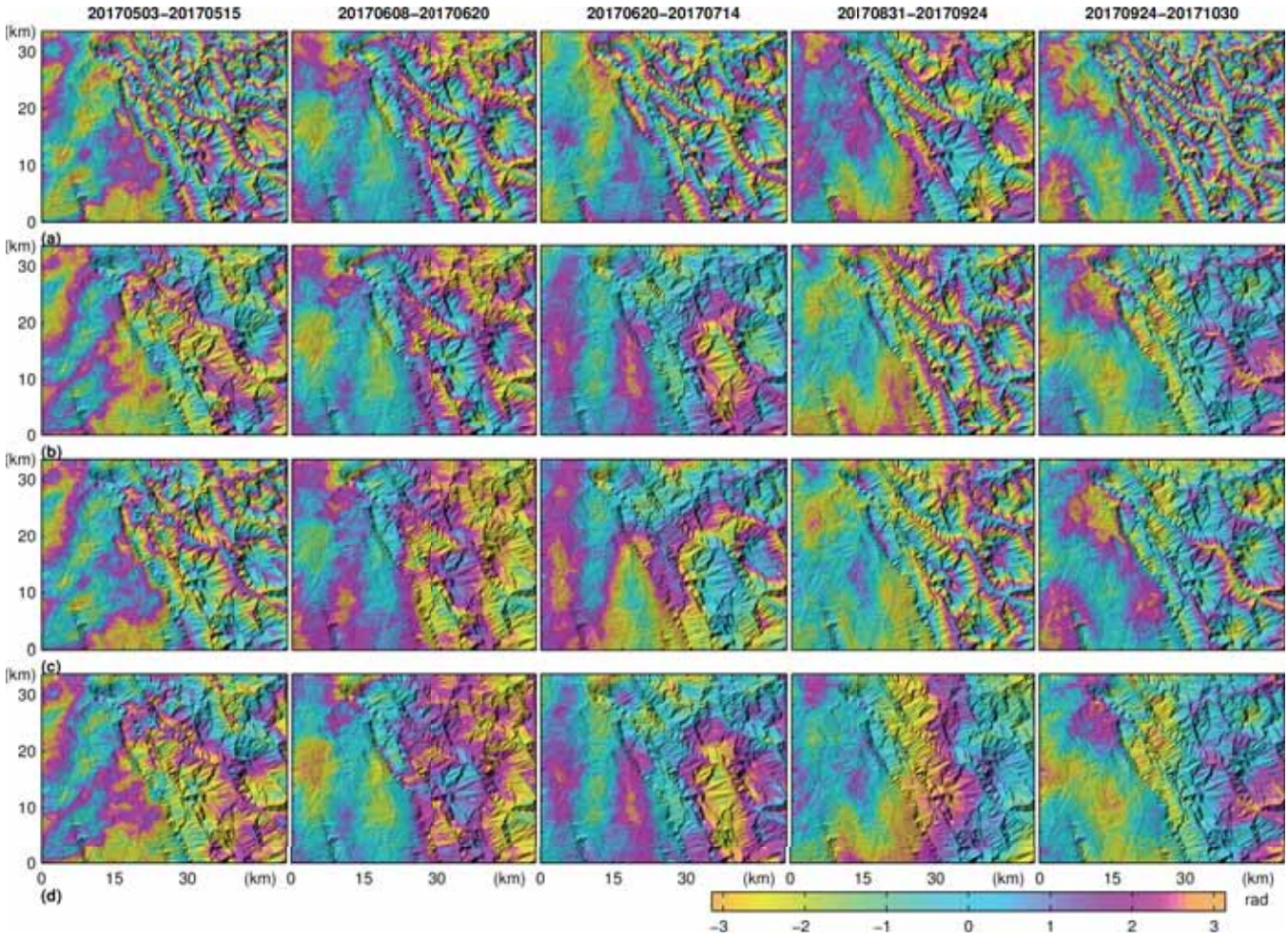

Fig. 11. Comparison of corrected interferograms over Iran–Iraq border for Sentinel-1 data. (a) Wrapped interferograms before correction TDs. (b) Wrapped interferograms after correction with linear method. (c) Wrapped interferograms after correction with ITD method. (d) Wrapped interferograms after correction with quadtree-aided joint model.

by the method proposed in [10] with sparsely sampled points, the interferogram scene was divided into local windows according to height gradient by quadtree. The smallest window size and the threshold of elevation range in the quadtree segmentation were set as 2.1 km and 1000 m, respectively. In each divided window, the stratified TDs were estimated jointly with the deformation rate and topographic error. Since this paper focuses on estimating and removing stratified TDs, qualitative validation and discussion of the deformation results are beyond the scope of this paper. Instead, we verified the effectiveness of TD correction of the proposed method through a comparison with a conventional linear method and iterative tropospheric decomposition (ITD) method [26]. In particular, the ITD method integrates high-resolution numerical weather model from the European Center for Medium-Range Weather Forecasts (ECMWF) with GPS-derived TD products (where available). The ITD approach has the capability of separating stratified and turbulent signals from tropospheric total delays and generating zenith total delay (ZTD) maps for correcting InSAR measurements. The combination of ECMWF and GPS ZTDs can preserve the attainable spatial and temporal resolutions of the two data sets. (For detailed information, please refer to http://ceg-research.ncl.ac.uk/v2/gacos/.)

Fig. 9 presents the wrapped phase maps after correcting TDs from the three methods for each interferometric pair. Fig. 9(a)–(d) illustrates the same series before correction, using the linear correction method, the ITD method, and our new quadtree aided joint model, respectively. It can be observed that in addition to other confounding signals (i.e., deformation, topographic error, and turbulence), the interferometric phases are mainly impacted by stratified TDs, which show a strong correlation with topography. After correcting TDs, all three methods lead to reduction in the global relation between topography and phase. However, discrepancies can still be observed between the tropospheric correction results over mountainous regions. The linear method leaves topography-related signals in the corrected interferometric pair 2008010–20080703 [Fig. 9(b)], while results corrected by ITD method show clear height-dependent patterns in interferometric pairs 20071001–20080101 and 20080101–20080703 [Fig. 9(c)]. By applying our proposed method, all corrected interferograms show the largest reduction of height-dependent signals among the three methods [Fig. 9(d)].

A statistical analysis on the delay/elevation ratios [37] was conducted to evaluate the performance of tropospheric correction. The ratios were calculated from local windows

TABLE II
AVERAGE LOCAL DELAY/ELEVATION RATIO (rad/km) BEFORE AND AFTER CORRECTIONS BEFORE AND AFTER LINEAR METHOD AND QUADTREE-AIDED JOINT MODEL

	20061229-20070213	20070213-20071001	20071001-20080101	20071001-20080216	20071001-20080703	20080101-20080216	20080101-20080703
Before correction	0.54	0.74	1.03	1.21	0.85	0.40	1.87
After first correction by linear method	0.53	0.58	0.42	0.52	0.53	0.39	0.58
After second correction by linear method	0.53	0.58	0.42	0.52	0.53	0.39	0.58
After first correction by joint model	0.48	0.49	0.28	0.42	0.47	0.35	0.47
After second correction by joint model	0.46	0.47	0.25	0.41	0.43	0.33	0.45

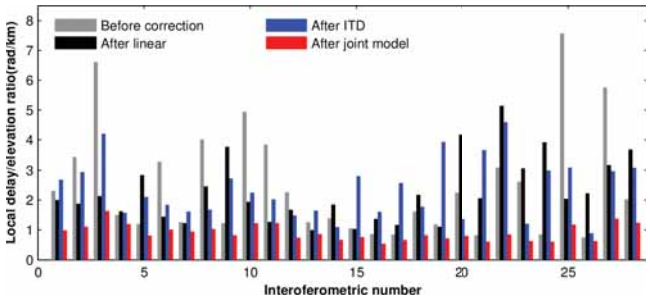

Fig. 12. Comparison of local delay/elevation ratios before and after corrections for Sentinel-1 data.

in unwrapped interferograms before and after TD correction. Fig. 10 presents the average delay/elevation ratio for each interferogram before and after corrections. It can be observed that all three methods show effectiveness in mitigating stratified TDs, while the proposed method yields the largest reduction in local delay/elevation ratios.

In addition, we also evaluate the correction performance under multiple iteration processes by the linear method and the proposed joint model. Table II presents the resulting delay/elevation ratios after the first and second corrections by these two methods, respectively. It can be seen that after the second correction, no improvement is found for the linear method and the improvement from the joint mode is also insignificant. This is because the majority of elevation-dependent delay has been removed in the first iteration. Considering the computational efficiency, one-time correction with the joint model is adequate to remove the height-related atmospheric delays.

B. Sentinel-1 Data Over Iran–Iraq Border

We further tested our method using C-band Sentinel-1 data over Iran–Iraq border where Mw 7.3 earthquake occurred on November 12, 2017. We used 19 Sentinel-1 images acquired between April 9, 2017 and November 11, 2017 to generate 28 interferograms. A total of 3 58 904 coherent points were selected from multilooked interferograms with a spatial resolution of around 50 m. The scene was divided into 337 local windows in which the joint estimation was implemented.

Fig. 11 provides a comparison of tropospheric correction results from 5 of 28 interferograms. The Sentinel-1 interferograms exhibit complicated phase patterns due to the spatial variation of stratified troposphere and possibly dramatic turbulence. The height-dependent TDs can be clearly observed in the mountainous areas. After tropospheric correction, all methods lead to reductions of height-dependent TDs. Fig. 12 presents the comparison of delay/elevation ratios before and after tropospheric correction for 28 interferograms. The results indicate that the proposed method can best remove the stratified TDs compared with the other two methods. It is worth noting that after correction, the nonzero delay/elevation ratios are attributed to the remaining confounding signals.

V. CONCLUSION AND DISCUSSION

In this paper, we proposed a quadtree-aided joint model for correcting stratified TDs under the MTInSAR framework. It has the capability of isolating TDs from wrapped interferometric phases despite the existence of deformation signal and topographic error. The key step of isolating confounding signals relies on the joint model which simultaneously estimates stratified TDs, deformation, and topographic error, therefore providing a more robust result. Meanwhile, accounting for the spatial variations of TDs, the joint model is performed within local windows, which are derived by quadtree segmentation according to the topography gradient.

The effectiveness of correcting TDs by the proposed method has been demonstrated by investigating both simulated and real SAR data sets extensively. The simulated experiments show that the joint estimation is robust against the interference of deformation and topographic error. The experiments also demonstrate that the quadtree-aided estimation is effective in lieu of the spatial variations of troposphere turbulence.

It is worth remarking that due to the dense network and strict phase ambiguity detector employed in the joint model [8], [10], the estimation of integer ambiguity is not necessary and phase unwrapping error can therefore be avoided. However, this is a thorny issue for the conventional linear method or external prediction product which is implemented based on the unwrapped phase of each interferometric pair.

In terms of computation efficiency, as the whole interferogram is divided into multiple windows, the computational memory and processing time can be high because of the joint estimation of intensive parameters and large redundant observations at arcs. Take the ALOS/PALSAR data for example, the whole processing files occupy about 17.1-GB memory. The processing time for this case is about 12.9 h on a desktop with an Intel i7 CPU and 64-GB memory. For the Sentinel-1 data case, the whole processing requires 6.7-GB memory and takes about 1.6 h utilizing MATLAB. The high demand for computation memory and processing time could be the main limitation of the proposed method. However, it is worth noting that the joint model is not only used for the correction of TDs. Considering the deformation and DEM errors are also simultaneously estimated from the model and further MTInSAR processing is no longer needed,

the high computation burden is acceptable. In future work, we plan to improve the algorithm efficiency by parallelizing the processing patch-wisely.

ACKNOWLEDGMENT

The authors would like to thank the Japan Aerospace Exploration Agency (JAXA) for providing the ALOS/PALSAR data and the European Space Agency for providing the Sentinel-1 data. The authors would also like to thank the anonymous reviewers for their constructive comments and suggestions.

REFERENCES

[1] Y. Fialko, "Evidence of fluid-filled upper crust from observations of postseismic deformation due to the 1992 M_w7.3 Landers earthquake," *J. Geophys. Res., Solid Earth*, vol. 109, no. B8, p. B08401, Aug. 2004.

[2] Z. Lu and D. Dzurisin, "InSAR imaging of aleutian volcanoes: Monitoring a volcanic arc from space," in *Springer Praxis Books, Geophysical Sciences*. New York, NY, USA: Springer, 2014, p. 390.

[3] Q. Sun, L. Zhang, X. Ding, J. Hu, Z. W. Li, and J. J. Zhu, "Slope deformation prior to Zhouqu, China landslide from InSAR time series analysis," *Remote Sens. Environ.*, vol. 156, pp. 45–57, Jan. 2015.

[4] R. M. Goldstein, H. Engelhardt, B. Kamb, and R. M. Frolich, "Satellite radar interferometry for monitoring ice sheet motion: Application to an antarctic ice stream," *Science*, vol. 262, no. 5139, pp. 1525–1530, 1993.

[5] L. Zhang, Z. Lu, X. Ding, H.-S. Jung, G. Feng, and C.-W. Lee, "Mapping ground surface deformation using temporarily coherent point SAR interferometry: Application to Los Angeles Basin," *Remote Sens. Environ.*, vol. 117, pp. 429–439, Feb. 2012.

[6] A. Ferretti, C. Prati, and F. Rocca, "Permanent scatterers in SAR interferometry," *IEEE Trans. Geosci. Remote Sens.*, vol. 39, no. 1, pp. 8–20, Jan. 2001.

[7] P. Berardino, G. Fornaro, R. Lanari, and E. Sansosti, "A new algorithm for surface deformation monitoring based on small baseline differential SAR interferograms," *IEEE Trans. Geosci. Remote Sens.*, vol. 40, no. 11, pp. 2375–2383, Nov. 2002.

[8] L. Zhang, X. Ding, and Z. Lu, "Modeling PSInSAR time series without phase unwrapping," *IEEE Trans. Geosci. Remote Sens.*, vol. 49, no. 1, pp. 547–556, Jan. 2011.

[9] A. Hooper, H. Zebker, P. Segall, and B. Kampes, "A new method for measuring deformation on volcanoes and other natural terrains using InSAR persistent scatterers," *Geophys. Res. Lett.*, vol. 31, no. 23, p. L23611, Dec. 2004.

[10] L. Zhang, X. Ding, Z. Lu, H.-S. Jung, J. Hu, and G. Feng, "A novel multitemporal InSAR model for joint estimation of deformation rates and orbital errors," *IEEE Trans. Geosci. Remote Sens.*, vol. 52, no. 6, pp. 3529–3540, Jun. 2014.

[11] L. Zhang, X. Ding, and Z. Lu, "Ground deformation mapping by fusion of multi-temporal interferometric synthetic aperture radar images: A review," *Int. J. Image Data Fusion*, vol. 6, no. 4, pp. 289–313, Oct. 2015.

[12] H. A. Zebker, P. A. Rosen, and S. Hensley, "Atmospheric effects in interferometric synthetic aperture radar surface deformation and topographic maps," *J. Geophys. Res., Solid Earth*, vol. 102, no. B4, pp. 7547–7563, Apr. 1997.

[13] M. Béjar-Pizarro, A. Socquet, R. Armijo, D. Carrizo, J. Genrich, and M. Simons, "Andean structural control on interseismic coupling in the North Chile subduction zone," *Nature Geosci.*, vol. 6, no. 6, pp. 462–467, 2013.

[14] O. Cavalié, M.-P. Doin, C. Lasserre, and P. Briole, "Ground motion measurement in the Lake Mead area, Nevada, by differential synthetic aperture radar interferometry time series analysis: Probing the lithosphere rheological structure," *J. Geophys. Res.*, vol. 112, no. B3, p. B03403, 2007.

[15] O. Cavalié *et al.*, "Measurement of interseismic strain across the Haiyuan fault (Gansu, China), by InSAR," *Earth Planet. Sci. Lett.*, vol. 275, nos. 3–4, pp. 246–257, Nov. 2008.

[16] J. R. Elliott, J. Biggs, B. Parsons, and T. J. Wright, "InSAR slip rate determination on the Altyn Tagh Fault, northern Tibet, in the presence of topographically correlated atmospheric delays," *Geophys. Res. Lett.*, vol. 35, no. 12, p. L12309, 2008.

[17] R. J. Walters, J. R. Elliott, Z. Li, and B. Parsons, "Rapid strain accumulation on the Ashkabad fault (Turkmenistan) from atmosphere-corrected InSAR," *J. Geophys. Res., Solid Earth*, vol. 118, no. 7, pp. 3674–3690, 2013.

[18] R. J. Walters, B. Parsons, and T. J. Wright, "Constraining crustal velocity fields with InSAR for Eastern Turkey: Limits to the block-like behavior of Eastern Anatolia," *J. Geophys. Res., Solid Earth*, vol. 119, no. 6, pp. 5215–5234, 2014.

[19] R. F. Hanssen, *Radar Interferometry: Data Interpretation and Error Analysis* (Remote Sensing and Digital Image Processing). Dordrecht, The Netherlands: Springer, 2001, p. 308.

[20] M.-P. Doin, C. Lasserre, G. Peltzer, O. Cavalié, and C. Doubre, "Corrections of stratified tropospheric delays in SAR interferometry: Validation with global atmospheric models," *J. Appl. Geophys.*, vol. 69, no. 1, pp. 35–50, Sep. 2009.

[21] E. Chapin *et al.*, "Impact of the ionosphere on an L-band space based radar," in *Proc. IEEE Conf. Radar*, Apr. 2006, p. 8.

[22] B. Zhang, X. Ding, W. Zhu, C. Wang, L. Zhang, and Z. Liu, "Mitigating ionospheric artifacts in coseismic interferogram based on offset field derived from ALOS-PALSAR data," *IEEE J. Sel. Topics Appl. Earth Observ. Remote Sens.*, vol. 9, no. 7, pp. 3050–3059, Jul. 2016.

[23] R. Jolivet *et al.*, "Improving InSAR geodesy using Global Atmospheric Models," *J. Geophys. Res. Solid Earth*, vol. 119, no. 3, pp. 2324–2341, 2014.

[24] J. Foster, B. Brooks, T. Cherubini, C. Shacat, S. Businger, and C. L. Werner, "Mitigating atmospheric noise for InSAR using a high resolution weather model," *Geophys. Res. Lett.*, vol. 33, no. 16, p. L16304, 2006.

[25] F. Onn and H. A. Zebker, "Correction for interferometric synthetic aperture radar atmospheric phase artifacts using time series of zenith wet delay observations from a GPS network," *J. Geophys. Res.*, vol. 111, no. B9, p. B09102, 2006.

[26] C. Yu, N. T. Penna, and Z. Li, "Generation of real-time mode high-resolution water vapor fields from GPS observations," *J. Geophys. Res., Atmos.*, vol. 122, no. 3, pp. 2008–2025, 2017.

[27] Z. Li, E. J. Fielding, P. Cross, and J.-P. Muller, "Interferometric synthetic aperture radar atmospheric correction: GPS topography-dependent turbulence model," *J. Geophys. Res., Solid Earth*, vol. 111, no. B2, p. B02404, 2006.

[28] Z. Li, J.-P. Muller, P. Cross, P. Albert, J. Fischer, and R. Bennartz, "Assessment of the potential of MERIS near-infrared water vapour products to correct ASAR interferometric measurements," *Int. J. Remote Sens.*, vol. 27, no. 2, pp. 349–365, 2006.

[29] Z. Li, E. J. Fielding, P. Cross, and J.-P. Muller, "Interferometric synthetic aperture radar atmospheric correction: Medium Resolution Imaging Spectrometer and Advanced Synthetic Aperture Radar integration," *Geophys. Res. Lett.*, vol. 33, no. 6, p. L06816, 2006.

[30] B. Puysségur, R. Michel, and J.-P. Avouac, "Tropospheric phase delay in interferometric synthetic aperture radar estimated from meteorological model and multispectral imagery," *J. Geophys. Res.*, vol. 112, no. B5, p. B05419, 2007.

[31] Z. Li, J.-P. Muller, P. Cross, and E. J. Fielding, "Interferometric synthetic aperture radar (InSAR) atmospheric correction: GPS, Moderate Resolution Imaging Spectroradiometer (MODIS), and InSAR integration," *J. Geophys. Res.*, vol. 110, no. B3, p. B03410, 2005.

[32] Y.-N. N. Lin, M. Simons, E. A. Hetland, P. Muse, and C. DiCaprio, "A multiscale approach to estimating topographically correlated propagation delays in radar interferograms," *Geochem., Geophys., Geosyst.*, vol. 11, no. 9, p. Q09002, 2010.

[33] X.-L. Ding, Z.-W. Li, J.-J. Zhu, G.-C. Feng, and J.-P. Long, "Atmospheric effects on InSAR measurements and their mitigation," *Sensors*, vol. 8, no. 9, pp. 5426–5448, Sep. 2008.

[34] D. P. S. Bekaert, R. J. Walters, T. J. Wright, A. J. Hooper, and D. J. Parker, "Statistical comparison of InSAR tropospheric correction techniques," *Remote Sens. Environ.*, vol. 170, pp. 40–47, Dec. 2015.

[35] D. A. Schmidt, R. Bürgmann, R. M. Nadeau, and M. d'Alessio, "Distribution of aseismic slip rate on the Hayward fault inferred from seismic and geodetic data," *J. Geophys. Res.*, vol. 110, no. B8, p. B08406, 2005.

[36] D. A. Schmidt and R. Bürgmann, "Time-dependent land uplift and subsidence in the Santa Clara valley, California, from a large interferometric synthetic aperture radar data set," *J. Geophys. Res., Solid Earth*, vol. 108, no. B9, p. 2416, 2003.

[37] D. P. S. Bekaert, A. Hooper, and T. J. Wright, "A spatially variable power law tropospheric correction technique for InSAR data," *J. Geophys. Res., Solid Earth*, vol. 120, no. 2, pp. 1345–1356, 2015.

[38] J. Biggs, T. Wright, Z. Lu, and B. Parsons, "Multi-interferogram method for measuring interseismic deformation: Denali fault, Alaska," *Geophys. J. Int.*, vol. 170, no. 3, pp. 1165–1179, Sep. 2007.
[39] J. Biggs *et al.*, "The postseismic response to the 2002 *M* 7.9 Denali Fault earthquake: Constraints from InSAR 2003–2005," *Geophys. J. Int.*, vol. 176, no. 2, pp. 353–367, 2009.
[40] B. Zhu, J. Li, Z. Chu, W. Tang, B. Wang, and D. Li, "A robust and multi-weighted approach to estimating topographically correlated tropospheric delays in radar interferograms," *Sensors*, vol. 16, no. 7, p. 1078, Jul. 2016.
[41] H. Fattahi and F. Amelung, "DEM error correction in InSAR time series," *IEEE Trans. Geosci. Remote Sens.*, vol. 51, no. 7, pp. 4249–4259, Jul. 2013.
[42] D. C.-L. Fong and M. Saunders, "LSMR: An iterative algorithm for sparse least-squares problems," *SIAM J. Sci. Comput.*, vol. 33, no. 5, pp. 2950–2971, 2011.
[43] K. Mogi, "Relations between the eruptions of various volcanoes and the deformations of the ground surfaces around them," *Bull. Earthq. Res. Inst.*, vol. 36, pp. 99–134, Jan. 1958.
[44] B. M. Kampes, *Radar Interferometry: Persistent Scatterer Technique*. Dordrecht, The Netherlands: Springer, 2006.
[45] W. Gan *et al.*, "Present-day crustal motion within the Tibetan Plateau inferred from GPS measurements," *J. Geophys. Res.*, vol. 112, no. B8, p. B08416, 2007.
[46] C. Wang, X. Ding, Q. Li, and M. Jiang, "Equation-based InSAR data quadtree downsampling for earthquake slip distribution inversion," *IEEE Geosci. Remote Sens. Lett.*, vol. 11, no. 12, pp. 2060–2064, Dec. 2014.

Hongyu Liang (S'18) was born in Bazhong, China, in 1991. He received the B.S. degree from Southwest Jiaotong University, Chengdu, China, in 2013, and the M.Sc. degree in geomatics from The Hong Kong Polytechnic University, Hong Kong, in 2013, where he is currently pursuing the Ph.D. degree with the Department of Land Surveying and Geo-Informatics.

His research interests include estimation theory and advanced processing developments for multitemporal synthetic aperture radar interferometry and deformation monitoring.

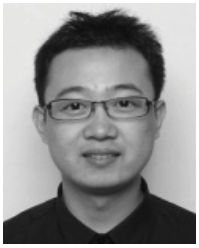

Lei Zhang (S'08–M'11) was born in Yantai, China, in 1981. He received the M.Sc. degree from Tongji University, Shanghai, China, in 2007, and the Ph.D. degree in geodesy and geodynamics from The Hong Kong Polytechnic University, Hong Kong, in 2011. His master's thesis was on fault slip inversion with interferometric synthetic aperture radar (SAR) and GPS data based on a triangular dislocation model.

Since 2012, he has been a Research Assistant Professor with the Department of Land Surveying and Geo-Informatics, The Hong Kong Polytechnic University. His research interests include developing advanced processing techniques for SAR data and the application of multitemporal interferometric analysis on the retrieval of ground displacement and geophysical parameters, with an emphasis on natural hazard monitoring and mitigation.

Xiaoli Ding received the B.S. degree from Central South University, Changsha, China, in 1983, and the Ph.D. degree from The University of Sydney, Sydney, NSW, Australia, in 1993.

He is currently the Chair Professor of geomatics and the Associate Dean of the Faculty of Construction and Environment, The Hong Kong Polytechnic University, Hong Kong. His research interests include developing technologies for studying ground and structural deformation and geohazards, with a current focus being upon spaceborne geodetic technologies such as GPS and interferometric synthetic aperture radar. He has authored over 300 papers in these research fields.

Prof. Ding is a fellow of the International Association of Geodesy (IAG). He is the President of Sub-Commission 4.4 of the IAG on airborne and spaceborne imaging technologies.

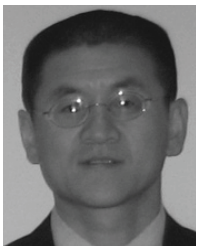

Zhong Lu (S'96–A'97–M'97–SM'07) received the B.S. and M.S. degrees from Peking University, Beijing, China, in 1989 and 1992, respectively, and the Ph.D. degree from the University of Alaska Fairbanks, Fairbanks, AK, USA, in 1996.

He was a Physical Scientist with the U.S. Geological Survey (USGS), Reston, VA, USA, from 1997 to 2013. He is currently a Professor and the Endowed Shuler-Foscue Chair with the Huffington Department of Earth Sciences, Southern Methodist University, Dallas, TX, USA. He is also a Principal Investigator of projects funded by NASA, ESA, JAXA, DLR, and USGS on the study of land surface deformation using satellite interferometric synthetic aperture radar (InSAR) imagery. He has authored or co-authored over 45 and 90 peer-reviewed journal articles and book chapters focused on InSAR techniques and applications. He has authored a book *InSAR Imaging of Aleutian Volcanoes: Monitoring a Volcanic Arc From Space*(Springer, 2014). His research interests include technique developments of SAR, InSAR, and persistent scatterer InSAR processing and their applications on natural hazard monitoring and natural resource characterization.

Dr. Lu is a Committee Member of the International User Team for Radarsat-C SAR Constellations, the GeoEarthscope InSAR User Working Group, the NASA's Alaska Satellite Facility User Working Group, and the upcoming NASA-India SAR Science Definition Team. He is also a member of the editorial boards of the *International Journal of Image and Data Fusion, Geomatics, Natural Hazards and Risk, andDatasetPapers in Geosciences*. He was a recipient of the American Society for Photogrammetry and Remote Sensing Award for Best Scientific Paper in *Remote Sensing*, the NASA Group Achievement Award, the NASA Certificate of Appreciation, the Raytheon Distinguished Level Award for Excellence in Technology, Science Applications, International Corporation Technical Fellow, and the Jerald Cook Memorial Award. He is the Chair of the Western North America InSAR Consortium. He is an Associate Editor of *Remote Sensing and Frontier in Volcanology*.

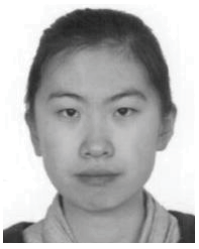

Xin Li was born in Tai'an, Shandong, China, in 1990. She received B.S. degree in geography information science from the Shandong University of Science and Technology, Qingdao, Shandong, China, in 2012, and the M.S. degree in the geoinformation science from the Chinese University of Hong Kong, Hong Kong, in 2013, where she is currently pursuing the Ph.D. degree with the Department of Land Surveying and Geo-Informatics, with a focus on atmosphere pollution analysis and prediction using remote sensing..

Her research interests include the atmospheric remote sensing application and spatial–temporal analysis.